



RESEARCH ARTICLE

10.1029/2020JB020539

Key Points:

- We propose a constitutive model that spans the brittle-ductile transition of basalt
- Through numerical simulations, we study the mechanisms of deformation in the basaltic crust
- Our results show that basalt is likely to exhibit brittle features at high temperature

Correspondence to:

F. Parisio,
francesco.parisio@protonmail.com

Citation:

Parisio, F., Lehmann, C., & Nagel, T. (2020). A model of failure and localization of basalt at temperature and pressure conditions spanning the brittle-ductile transition. *Journal of Geophysical Research: Solid Earth*, 125, e2020JB020539. <https://doi.org/10.1029/2020JB020539>

Received 6 JUL 2020

Accepted 7 OCT 2020

Accepted article online 10 OCT 2020

A Model of Failure and Localization of Basalt at Temperature and Pressure Conditions Spanning the Brittle-Ductile Transition

Francesco Parisio^{1,2} , Christoph Lehmann³, and Thomas Nagel^{1,2} 

¹Chair of Soil Mechanics and Foundation Engineering, Technische Universität Bergakademie Freiberg, Freiberg, Germany, ²TUBAF-UFZ Center for Environmental Geosciences, Freiberg, Germany, ³Department of Environmental Informatics, Helmholtz Centre for Environmental Research-UFZ, Leipzig, Germany

Abstract Natural phenomena such as seismicity, volcanism, and fluid circulation in volcanic areas are influenced by the mechanical response of intact basalt. When subjected to a wide range of environmental loading conditions, basalt exhibits inelastic deformation characteristics ranging from brittle to ductile behavior. In this manuscript, we present a new constitutive model of basalt that spans the brittle-ductile transition by covering a wide range of mean effective stress, temperature, and strain rate. The model has been implemented into the automatic constitutive model code generator MFront, which we have coupled with the finite element solver OpenGeoSys. The software employed for the computations is open source, accessible and offers a versatile solution to model thermomechanical failure of rocks. Within this framework, we have performed numerical simulations that highlight the localization of strains and stresses under triaxial compression. Predictions of the constitutive response, of the depth of the brittle-ductile transition, and of the localization patterns are in agreement with laboratory and in situ observations. The results have important geophysical implications as they provide a constitutive basis that explains the mechanisms through which basalt can deform in a brittle fashion at temperatures above 600°C.

1. Introduction

Deformation of intact rock under loading controls the development of fractures and faults in the Earth's crust, which in turn influence natural phenomena such as earthquakes (Ohnaka, 2003; Pec et al., 2016; Shimamoto & Noda, 2014), volcanic eruptions (Bakker et al., 2015; Benson et al., 2008; Heap et al., 2013; Lavallée et al., 2019), and hydrothermal circulation (Lamur et al., 2017; Violay et al., 2017; Watanabe et al., 2017). The mechanisms that control the deformation of intact rock under shearing depend on environmental variables, such as the acting temperature, stress, and strain rate (Kato et al., 2004; Kumari et al., 2017; Odedra et al., 2001; Ohnaka, 1995; Violay et al., 2012; Wong, 1982). As temperature rises with depth, it influences the solid and fluid rheology and their interaction, and as a result the environmental effects are even more relevant in the deep part of the crust and in regions where the geothermal gradient is above average, such as volcanic areas (Parisio et al., 2019). The deformation characteristics of rocks can determine the (potential) maximum depth at which earthquakes can be expected: While several have placed the limit at 600°C (references within Molnar, 2020), evidence suggests that such a limit is likely to be arbitrary and that earthquakes could be expected in the hot crust at ~800°C (Molnar, 2020). Further support to this hypothesis seems to come from laboratory experiments that have shown that basaltic rocks exhibit acoustic emission in what is usually considered the ductile deformation regime (Adelinet et al., 2013). In this contribution, we propose a constitutive model of basalt, a typical rock of volcanic provinces, that spans a wide range of temperature, pressure, and strain rate. We employ numerical simulations to study the implications of the rheology of basalt on the formation of fractures and shear zones.

The mechanical behavior of rocks is commonly split between two idealized limits (Evans et al., 1990; Karato, 2008; Karato & Wong, 1995): On the one hand, the brittle behavior is characterized by high strength, dilatancy at fracture onset, microcracking growth and accumulation (eventually, rate-dependent, cf. Brantut et al., 2013), strain softening, and localized deformation (Hori & Nemat-Nasser, 1986; Lockner et al., 1991; Violay et al., 2012). Brittle deformation is therefore most commonly observed at low temperature and pressure and high strain rate. On the other hand of the spectrum, the ductile behavior is characterized by a lower

©2020. The Authors.

This is an open access article under the terms of the Creative Commons Attribution License, which permits use, distribution and reproduction in any medium, provided the original work is properly cited.

strength, intragranular or intergranular plasticity, thermally activated viscous dissipation, strain hardening followed by perfect plasticity, and diffused deformation (Bakker et al., 2015; Karato & Wong, 1995; Reber & Pec, 2018). Some minerals such as feldspar interpose an intermediate phase of diffused microcracking and cataclastic flow to the transition between faulting and temperature-activated crystal plasticity (Tullis & Yund, 1992). Ductility increases with temperature and pressure and is inversely proportional to strain rate. The transition between the brittle and the ductile ends of the spectrum is usually referred to as the brittle-ductile transition (BDT) and does not characterize a singularity in the Earth's crust but instead a transition zone where one inelastic deformation mechanism gradually becomes dominant over another (Aharonov & Scholz, 2019; Meyer et al., 2019).

Basalt is the most abundant igneous rock on Earth forming large portions of the oceanic crust (Violay et al., 2012) and of active volcanic areas and flood basalt provinces in the continental crust (Ross et al., 2005). Analogous to other rocks, basalt deformation in brittle conditions is associated with stress drops and localized faulting (Violay et al., 2012). Microcracking induces dilatancy, elastic wave velocity reduction, and acoustic emission associated with shear-type events (Adelinet et al., 2013). At increasingly ductile deformation behavior, stress drops disappear and diffused-mode hardening plasticity occurs along with compaction-induced acoustic emissions (Adelinet et al., 2013). Temperature increase promotes solid-state diffusion activating creep and rate-dependent permanent strain (Violay et al., 2012). Volumetric strain and porosity decrease gradually transition toward isochoric inelastic deformation at high temperature (Violay et al., 2015). Since crack growth governs a large portion of the inelastic deformation of rocks (Horii & Nemat-Nasser, 1986) until solid-state diffusion is activated, models based on damage mechanics that include permanent and rate-dependent deformation can successfully describe the processes that lead to the formation of fractures and faults (Jacquey & Cacace, 2020; Lyakhovsky et al., 1997, 2011; Parisio et al., 2019). Although several models have been specifically developed for isothermal conditions or for highly porous rocks, a comprehensive model of basalt that spans a wide range of temperature, pressure, and strain rate is still missing, mostly as a consequence of the difficulties associated in testing basalt at high temperature and confining stress (Caristan, 1982; Kronenberg & Shelton, 1980; Marti et al., 2017)—a fundamental ingredient to build detailed evidence that forms the base of constitutive models.

In this contribution, we wish to fill this gap and we propose a modeling framework for the rheology of basalt that spans the BDT conditions in terms of temperature, pressure, and strain rate. We have formulated a coupled model of damage-plasticity-creep which depends on all three variables. The model is integrated into the automatic code generator MFronT (Helfer et al., 2015, 2020), which is coupled with the FEM code OpenGeoSys (Bilke et al., 2019; Kolditz et al., 2012; Yoshioka et al., 2019) to solve thermomechanical boundary value problems. We have analyzed the constitutive response of the model calibrated against a set of laboratory experiments in triaxial conditions (Violay et al., 2012). We have employed the calibrated parameters to systematically study the model response in terms of strength, damage accumulation, localization, and dissipated energy and to map the BDT in the $\sigma_m - T - \dot{\epsilon}$ space. We have investigated the consequences of our findings in terms of the BDT depth and its relation with recorded seismicity. Our results show that localized failure and stress drops are possible beyond the 600°C limit.

2. Constitutive Model

We have based our modeling on high-pressure and high-temperature triaxial experiments on Escandorgue Basalt, which are available in the literature (Violay et al., 2012) and have been previously employed for the formulation of a plastic yield surface spanning the BDT (Parisio et al., 2019). Escandorgue Basalt is a columnar basalt from the Escandorgue flow in France and has a porosity of approximately 0.023 (Violay et al., 2012). In the experiments by Violay et al. (2012), confining pressures of 100 to 300 MPa were applied to specimens heated to temperatures between 400°C and 950°C. This high-confinement and high-temperature range rendered this an ideal experimental data set to fit our model to.

2.1. Mathematical Formulation

The problem is formulated in terms of the primary variables temperature T and displacement \mathbf{u} , and the system of partial differential equations is formulated through the balance relations for energy and linear momentum. The former reduces here to the heat conduction equation

$$\varrho c_p \frac{dT}{dt} - \nabla \cdot (\lambda \nabla T) = 0, \quad (1)$$

while for the latter the general form

$$\nabla \cdot \boldsymbol{\sigma} + \varrho \mathbf{g} = \mathbf{0} \quad (2)$$

was chosen. In the above, $\varrho = 2,900 \text{ kg m}^{-3}$ is the rock density (Violay et al., 2012), $c_p = 840 \text{ J kg}^{-1} \text{ K}^{-1}$ is its isobaric specific heat capacity, $\lambda = 1.71 \text{ W m}^{-1} \text{ K}^{-1}$ is the isotropic thermal conductivity, and \mathbf{g} is the gravity acceleration vector (gravitational effects are neglected in our calculations due to small sample sizes). The selected values of specific heat and thermal conductivity are within a typical range for basaltic rock (Hartlieb et al., 2016).

The Young's modulus is assumed to be temperature dependent, with the following quadratic expression:

$$E = E_0 [a_E \langle T - 673.15 \text{ K} \rangle^2 + b_E \langle T - 673.15 \text{ K} \rangle + c_E], \quad (3)$$

where $a_E = -2.169 \times 10^{-6} \text{ K}^{-2}$, $b_E = -1.644 \times 10^{-4} \text{ K}^{-1}$, and $c_E = 9.681 \times 10^{-1}$ are parameters determined on the elastic part of the stress strain curve of the experimental results and $E_0 = 44.62 \text{ GPa}$. In the above, the Macauley brackets $\langle \bullet \rangle$ have been used. To calibrate the empirical nonlinear relationship between Young's modulus and temperature, tests must be performed at a minimum of three different values of temperature.

The total strain tensor is the symmetric part of the displacement gradient:

$$\boldsymbol{\epsilon} = \frac{1}{2} [\nabla \mathbf{u} + (\nabla \mathbf{u})^T], \quad (4)$$

and is split into elastic $\boldsymbol{\epsilon}^e$, plastic $\boldsymbol{\epsilon}^p$, viscous $\boldsymbol{\epsilon}^v$, and thermal $\boldsymbol{\epsilon}^{\text{th}}$ contributions:

$$\boldsymbol{\epsilon} = \boldsymbol{\epsilon}^e + \boldsymbol{\epsilon}^p + \boldsymbol{\epsilon}^v + \boldsymbol{\epsilon}^{\text{th}}, \text{ with } \boldsymbol{\epsilon}^{\text{th}} = \alpha_T \Delta T \mathbf{I}. \quad (5)$$

Here, $\Delta T = T - T_0$ measures the local temperature change from reference conditions and α_T denotes the linear thermal expansion coefficient.

Damage d is introduced in the constitutive description through the damage-effective stress tensor $\tilde{\boldsymbol{\sigma}}$ defined as

$$\tilde{\boldsymbol{\sigma}} = \frac{\boldsymbol{\sigma}}{(1 - d)}, \quad (6)$$

which can be interpreted as the stress acting on the undamaged part of the solid. The constitutive equation relates this damage-effective stress tensor to the elastic strain tensor as

$$\tilde{\boldsymbol{\sigma}} = K(\text{tr} \boldsymbol{\epsilon}^e) \mathbf{I} + 2G \boldsymbol{\epsilon}_D^e, \quad (7)$$

with $\boldsymbol{\epsilon}_D^e$ the deviator of the elastic strain tensor, $K = E/[3(1 - 2\nu)]$ is the solid's bulk modulus, $G = E/[2(1 + \nu)]$ is its shear modulus, and ν its Poisson's ratio. The final expression of the constitutive equation writes

$$\boldsymbol{\sigma} = (1 - d)K[\text{tr}(\boldsymbol{\epsilon} - \boldsymbol{\epsilon}^p - \boldsymbol{\epsilon}^v) - 3\alpha_T \Delta T] \mathbf{I} + (1 - d)2G(\boldsymbol{\epsilon}_D - \boldsymbol{\epsilon}_D^p - \boldsymbol{\epsilon}_D^v), \quad (8)$$

where the internal variables are the rate-independent plastic strain, the rate-dependent viscous strain, and damage. The evolution equation of the plastic strain tensor is given by the plastic flow rule:

$$\frac{d\boldsymbol{\epsilon}^p}{dt} = \dot{\lambda}^p \frac{\partial \mathbf{g}^p}{\partial \tilde{\boldsymbol{\sigma}}}, \quad (9)$$

where the gradient of the plastic flow potential \mathbf{g}^p in damage-effective stress space gives the direction of the plastic strain rate, while its magnitude is determined by the plastic multiplier $\dot{\lambda}^p$. For associated

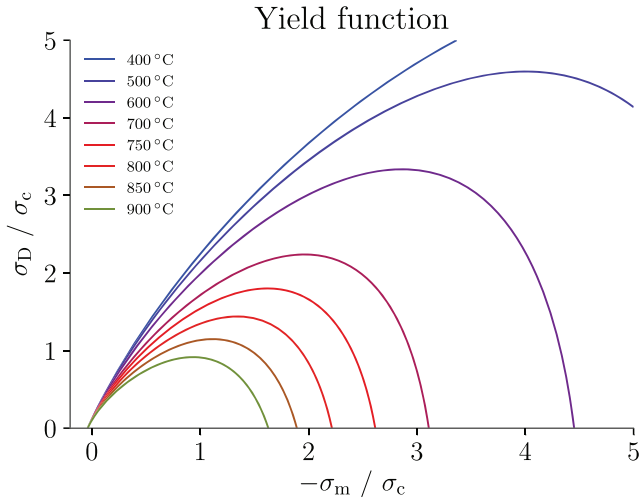


Figure 1. Yield failure in the mean versus deviatoric stress space. The temperature increase shrinks the yield function and degrades the available strength at higher confinement.

plasticity, the plastic potential g^p is taken as equal to the yield function f^p and the loading-unloading conditions (Karush-Kuhn-Tucker conditions) write

$$f^p \leq 0; \quad \dot{\lambda}^p \geq 0; \quad \dot{\lambda}^p f^p = 0. \quad (10)$$

The plastic yield surface is a function of the invariants of the effective stress tensor, namely, the deviatoric (von Mises equivalent) $\tilde{\sigma}_D$ and the mean stress $\tilde{\sigma}_m$, which are defined as

$$\tilde{\sigma}_m = \frac{1}{3} \text{tr}(\tilde{\sigma}); \quad \tilde{\sigma}_D = \sqrt{\frac{3}{2} \tilde{\sigma}_D : \tilde{\sigma}_D}, \quad (11)$$

where $\tilde{\sigma}_D = \tilde{\sigma} - \text{tr}(\tilde{\sigma})\mathbf{I}/3$. The expression of the yield surface (Figure 1) is an extension of the Hoek-Brown model (Grassl & Jirásek, 2006), which was previously employed to characterize the BDT of rocks (Parisio et al., 2019), and reads

$$f^p = \left[(1 - q_h) \left(\frac{\tilde{\sigma}_D}{3\sigma_c} + \frac{\tilde{\sigma}_m}{\sigma_c} \right)^2 + \frac{\tilde{\sigma}_D}{\sigma_c} \right]^2 + m_0 q_h^2 \left(\frac{\tilde{\sigma}_D}{3\sigma_c} + \frac{\tilde{\sigma}_m}{\sigma_c} \right) - q_h^2, \quad (12)$$

where $\sigma_c = 339$ MPa is the uniaxial compressive strength, $m_0 = 26.11$ is a frictional parameter, and $q_h(\epsilon^p, \epsilon^v, T)$ is a hardening variable defined as a function of the plastic and viscous strain tensor and temperature:

$$q_h(\epsilon^p, \epsilon^v, T) = \frac{R_p(\epsilon^p, \epsilon^v)}{[1 + (\alpha \Delta T)^n]^{(1 - \frac{1}{n})}}, \quad (13)$$

where $\alpha = 1.42 \times 10^{-3} \text{ K}^{-1}$ and $n = 4.72$ are responsible for the decrease of the yield strength with increasing temperature (thermal softening). The values of parameters σ_c , m_0 , α , and n were determined in a previous study (Parisio et al., 2019) and were based on the same experimental evidence for basalt considered in this study.

The function $R_p(\epsilon^p, \epsilon^v)$ defines the temperature-independent hardening evolution:

$$R_p(\epsilon^p, \epsilon^v) = \begin{cases} -(1 - q_{h0})\chi^2 + 2(1 - q_{h0})\chi + q_{h0} & \text{if } \chi \leq 1 \\ 1 & \text{if } \chi > 1 \end{cases}, \quad (14)$$

where $q_{h0} = 8.59 \times 10^{-1}$ is a parameter determining the initial value of the yield function (Parisio et al., 2019) and $\chi = (\epsilon_{\text{eff}}^p + \epsilon_{\text{eff}}^v)/R_v$, where variable $R_v = r_1 T + r_2 \sigma_m + r_3$ is a function scaling the amount of plastic strain hardening with pressure and temperature and where $r_1 = 1.1522 \cdot 10^{-4} \text{ K}^{-1}$, $r_2 = -9.4003 \cdot 10^{-5} \text{ MPa}^{-1}$, and $r_3 = -8.1075 \cdot 10^{-2}$. The viscous strain rate is of the Norton creep type and writes

$$\frac{d\epsilon^v}{dt} = \sqrt{\frac{3}{2}} A \exp\left(-\frac{Q}{RT}\right) \left(\frac{\tilde{\sigma}_D}{\sigma_{\text{ref}}}\right)^m \frac{\tilde{\sigma}_D}{\|\tilde{\sigma}_D\|}, \quad (15)$$

where $Q = 6.8 \cdot 10^5 \text{ J mol}^{-1}$ is the activation energy, $A = 8.0 \cdot 10^8 \text{ s}^{-1}$ is a material constant, $m = 6.8$ is the power law stress exponent, R is the universal gas constant, and $\sigma_{\text{ref}} = 1$ MPa is the reference deviatoric stress. The parameters characterizing the viscous strain rate were chosen to fit both the constant and varying strain-rate triaxial tests on Escandorgue Basalt (Violay et al., 2012) as a consequence of the nontrivial

Table 1

Parameters of the Constitutive Model

Type	Symbol	Value	Unit	Calibration
Thermoelastic law	E_0	4.462×10^{11}	GPa	A
	a_E	-2.169×10^{-6}	K^{-2}	A
	b_E	-1.644×10^{-4}	K^{-1}	A
	c_E	9.681×10^{-1}	—	A
Yield function	σ_c	3.390×10^2	MPa	B
	m_0	2.611×10^1	—	B
Thermal strength decay	α	1.420×10^{-3}	K^{-1}	B
	n	4.720×10^0	—	B
Plastic hardening	q_{h0}	8.590×10^{-1}	—	C
	r_1	1.152×10^{-4}	K^{-1}	C
	r_2	-9.400×10^{-5}	MPa^{-1}	C
	r_3	-8.108×10^{-2}	—	C
Creep	Q	6.800×10^5	$J mol^{-1}$	C
	A	8.000×10^8	s^{-1}	C
	m	6.800×10^0	—	C
	α_{dc}	3.000×10^{-2}	—	C
Damage	α_{dt}	3.000×10^{-5}	—	C

Note. Calibration obtained as follows: A = fitting of elastic law with T ; B = fitting yield surface (Parisio et al., 2019); and C = fitting the stress-strain curve from triaxial tests of Escandorgue Basalt (Violay et al., 2012).

interplay between creep, plasticity, and damage. The damage internal variable d is split between damage increment due to compression d_c and tension d_t :

$$d = 1 - (1 - d_c)(1 - d_t), \quad (16)$$

which have evolution equations depending on plastic strain as

$$\dot{d}_c = \exp\left(-\frac{\epsilon_{eff}^p + \epsilon_{eff}^v}{\alpha_{dc}}\right) \frac{(\epsilon_{eff}^p + \epsilon_{eff}^v) q_h^3 \langle \sigma_m \rangle^-}{\alpha_{dc} |\sigma_m|}, \quad (17)$$

and

$$\dot{d}_t = \exp\left[-\frac{\epsilon_{eff}^p}{\alpha_{dt}}\right] \frac{\epsilon_{eff}^p \langle \sigma_m \rangle^+}{\alpha_{dt} |\sigma_m|}, \quad (18)$$

where $\langle x \rangle^+$ and $\langle x \rangle^-$ represent the positive and negative Macaulay brackets, respectively. α_{dt} and α_{dc} are parameters defining the rate of softening (see Parisio & Laloui, 2017, for their meaning) and in this case $\alpha_{dc} = 3.00 \times 10^{-2}$ and $\alpha_{dt} = \alpha_{dc}/1,000$. Plasticity and creep are formulated in the damage effective stress space, which means damage evolution can be evaluated explicitly following the stress-return integration (Parisio et al., 2019).

Overall, the parameters describing the constitutive model were selected to fit the experimental behavior of Escandorgue Basalt and are summarized in Table 1. The thermoelastic parameters describing the evolution of Young's modulus with temperature can be obtained by fitting Equation 3 to the experimentally obtained stiffness. The calibration of the yield surface in the pressure and temperature space was discussed in detail in Parisio, Vinciguerra, et al. (2019). Finally, the calibration of the parameters controlling the evolution of the plastic, viscous, and damage internal variables was performed to fit the available stress-strain experimental curves in triaxial conditions (Violay et al., 2012).

2.2. Numerical Implementation

We have coupled the automatic integrator MFront (Helfer et al., 2015) with the finite element solver OpenGeoSys (Bilke et al., 2019; Kolditz et al., 2012), both of them open source, C++, object-oriented applications. For that purpose, the recently introduced generic interface support (MGIS) (Helfer, 2019; Helfer et al., 2020) has been used. Integration point-based state updates are handled via the MGIS interface such that OGS and MFront communicate consistently. The general algorithm follows a fully implicit

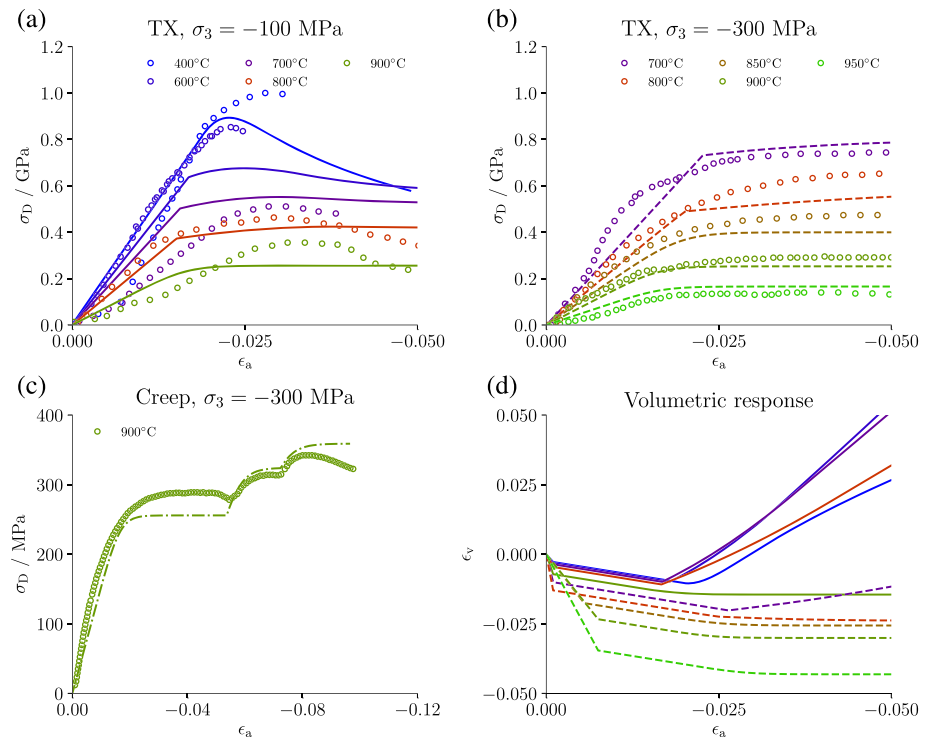


Figure 2. Comparison of model results (solid and dotted lines) against laboratory experiments (open dots, data from Violay et al., 2012) in triaxial configuration. Results are shown in terms of axial deformation versus equivalent Von Mises stress (a–c) and axial deformation versus volumetric deformation (d). The constitutive model fits well the experimental evidence over a range of confinement, temperature, and strain rate.

integration scheme with a consistently linearized nested multilevel Newton-Raphson scheme. In brief, the discretized linear momentum balance is linearized around a current state in order to iteratively update the current configuration estimate seeking to satisfy the equilibrium conditions. In order to calculate the internal nodal force vector, stresses at the integration points have to be determined corresponding to the current estimate of the displacement field change (and its rate). This stress determination, along with the integration of the constitutive model's internal state variables, is then performed by MFronT within the local (constitutive) Newton-Raphson loop. The algorithm then returns the new state to the finite element assembly routines along with the consistent material tangent. The stress and the tangent are then used to perform the next global Newton iteration. Consistency of both Newton schemes is required for quadratic convergence in the vicinity of the solution (de Borst & Heeres, 2002; Nagel et al., 2017).

3. Constitutive Response

The material parameters are calibrated through material point level simulations of the constitutive response against Escandorgue Basalt (Violay et al., 2012). All tests were performed in triaxial configuration at different confinement and temperature, with the addition of creep tests with nonconstant loading rate. The model can reproduce the experimental observations of the stress-strain behavior (Violay et al., 2012), including the influence of temperature and confining pressure variations (Figure 2). At low confinement (100 MPa, Figure 2a), the behavior is brittle at low temperature with minor plastic hardening followed by softening. The softening decreases with increasing temperature until the mechanical behavior is dominated by hardening plasticity without softening and the dissipation is purely viscoplastic above 800°C. The temperature increase affects the deviatoric behavior by decreasing strength and increasing ductility. At higher confinement (300 MPa, Figure 2b), the stress-strain response shows plastic hardening with decreasing values of deviatoric strength with temperature, which in turn activates creep following Norton's law at $T \geq 850^\circ\text{C}$.

The model correctly predicts the creep-dominated behavior above the activation temperature at increasing deformation rate (Figure 2c). The volumetric strain decreases during the initial elastic phase, and its rate

becomes either positive (dilatancy) or negative (compaction) at the onset of inelastic deformation. Dilatancy occurs at low confinement and temperature and becomes isochoric or even slightly compacting at higher values of temperature and pressure (Figure 2d). Although no record of volumetric strain of Escandorgue Basalt is available (porosity evolution can be found in Violay et al., 2015), the model predictions are in qualitative agreement with other experimental evidence at high pressure and temperature performed on granite (Violay et al., 2017). Isochoric inelastic deformations are observed when creep is activated.

4. Localized Deformation

Although not limited to softening materials, the presence of softening is often an indication for a strong tendency for strain localization (Hobbs et al., 1990). We briefly introduce a simplified technique based on energy dissipation that removes the mesh bias associated with such phenomena and subsequently study the model's predictions in terms of localized deformation.

4.1. Mesh-Adjusted Softening Behavior and Localization Indicator

Nonlocal models (Guy et al., 2018; Tvergaard & Needleman, 1995), micropolar continua (Suh et al., 2020; Zheng et al., 2016), gradient-damage models (de Borst & Verhoosel, 2016; Nguyen et al., 2018), enhanced-strain methods (Armero & Garikipati, 1996), viscoplastic regularization (Duretz et al., 2020; Simo & Ju, 1987), or other extended formulations are proven methods to mitigate the mesh-dependent effects (Parisio et al., 2019; Yoshioka et al., 2019). In this work, we apply a mesh-adjusted softening parameter α_d and all simulations are performed with the same discretization (quadrilateral elements of 0.5 mm size). The discretization-adjusted value of the softening parameter is derived by requiring the equivalence of dissipated energy between the limiting cases of a uniform strain field on the one hand and a strain field localized into a band of one element thickness on the other. The fracture energy depends on the constitutive parameters (Yoshioka et al., 2019):

$$G_c = g_f w_f = \left(\frac{\sigma_t^2}{2E} + \sigma_t \alpha_{dt} \right) w_f, \quad (19)$$

where g_f is the fracture energy per unit volume, w_f is the fracture width, and σ_t is the uniaxial tensile strength. The equivalence between fracture energy in uniform and localized condition writes

$$g_f w_f = g_f^* w_f^*, \quad (20)$$

with

$$g_f^* = \frac{\sigma_t^2}{2E} + \sigma_t \alpha_{dt}^*, \quad (21)$$

where the superscript $*$ refers to localized conditions. The value of the softening parameter in localized conditions is derived by combining Equation 20 with Equation 21 and writes

$$\alpha_{dt}^* = \frac{1}{\sigma_t} \left(g_f \frac{w_f}{w_f^*} - \frac{\sigma_t^2}{2E} \right). \quad (22)$$

The minimum and maximum deviatoric strains in the sample are a good quantitative indicator of how much the deviatoric deformation localizes within the sample. The deviatoric strain measure assumed is

$$\epsilon_D = \sqrt{\epsilon : \epsilon - \frac{1}{3}(\text{tr} \epsilon)^2}. \quad (23)$$

$\epsilon_{D,\max}$ and $\epsilon_{D,\min}$ are its minimum and maximum values within the sample, respectively. Their ratio $\bar{\epsilon}_D = \epsilon_{D,\max} / \epsilon_{D,\min}$ is employed to characterize the localized deformation: (i) $\bar{\epsilon}_D = 1$ implies that the deviatoric deformation is uniform; (ii) $\bar{\epsilon}_D > 1$ indicates that deformation is localized.

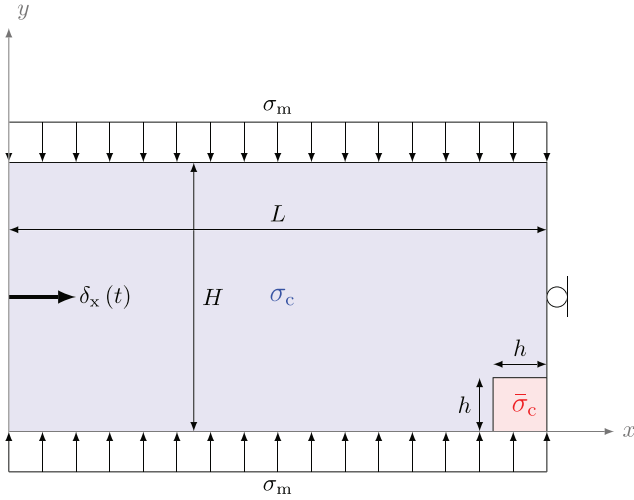


Figure 3. Schematic representation of the triaxial compression finite element models containing a defect that promotes localization. The sample has a height of $H = 10$ mm and length of $L = 20$ mm, while the defect is a small square of $h = 0.5$ mm side placed at the bottom right corner and with a uniaxial compressive strength of $\bar{\sigma}_c = 271.2$ MPa corresponding to an 80% reduction of the sample's value of $\sigma_c = 339.0$ MPa. The sample is subjected to a confining stress σ_m , which is constant and applied also in the out-of-plane direction, while the deviatoric loading is imposed through displacement boundary condition $\delta_x(t)$.

To study the localized deformation behavior across the brittle-ductile regimes of deformation, we perform FEM analyses with the coupled OGS-MFront solver in triaxial compression of finite-size specimens ($L = 0.02$ m, $H = 0.01$ m) at different confinement and temperature

$$\sigma_m \in \{-50, -150, -250, -350\} \text{ MPa}, \quad (24)$$

$$T \in \{400, 600, 800\} ^\circ\text{C}. \quad (25)$$

We have introduced a small square defect of the same size as the discretization $h = 0.5$ mm in the sample (Figure 3) as a reduction of the uniaxial compressive strength to 80% its original value; the objective is to enhance the appearance of a localized pattern (although it is a nonnecessary condition). The sample is in isothermal conditions at all times and the loading is first applied as an isotropic increase up to the prescribed confinement σ_m , with a following deviatoric phase controlled by displacement boundary condition $\delta_x(t)$, which corresponds to a loading rate of $\dot{\epsilon} = 10^{-5} \text{ s}^{-1}$ (Figure 3). The sample is loaded in triaxial configuration; that is, the out-of-plane component of stress is at all times equal to the prescribed confinement σ_m . The fracture-width ratio is computed as the ratio between the uniform case, where $w = L = 0.02$ m, and the one with element size of the 0.0005 m. The mesh-adjusted softening parameters employed for the finite element analyses are $\alpha_{dc}^* = 1.35$ and $\alpha_{dt}^* = 0.0098$, respectively, considering that $\sigma_t = 19.4$ MPa and $\sigma_c = 339.0$ MPa.

4.2. Localized Deformation Patterns Across the BDT

The deviatoric deformation map at a gross axial strain of ϵ_{xx} , $t = 0.08$ ($\delta_x = 0.0016$ m) strongly depends on the environmental conditions of pressure and temperature (Figure 4). The localization patterns are more evident at lower temperature and confinement, that is, toward the brittle regime. Confinement and temperature increase have the analogous effect of pushing the deformation pattern toward homogeneous conditions. At the ductile end of the spectrum, the defect in the sample decreases in relevance in terms of triggering localized deformation. For example, in ductile deformation conditions at confinement of 350 MPa, the defect triggers a clearly visible localized deformation pattern that disappears at $T \geq 600^\circ\text{C}$.

The angle between the direction of the shear band and the vertical direction decreases with increasing confinement and temperature, that is, with a shift toward ductile deformation. The experimental results yielded a splitting failure pattern with a localization band inclination of approximately $\sim 58.4^\circ$ at 100 MPa of confinement and up to a temperature of 700°C , while shear failure and localized plastic shear orientation $\sim 50.7^\circ$ was observed up to 900°C at 100 MPa and up to 800°C at 300 MPa (Violay et al., 2012). The numerical simulations correctly reproduces the trend toward a reduction of the shear band inclination with increased ductility.

Figure 5 shows the stress-strain response and the localized deviatoric strain measure $\bar{\epsilon}_D$ at different confinement and temperature. The environmental influence on the stress-strain response of the FEM model has a similar trend when compared to one of the constitutive response analyzed at material point level (i.e., no localized deformation as in Figure 2). Strength decreases with temperature and increases with confinement, while the damage-induced strain softening decreases gradually with increasing confinement and temperature until the response is purely viscoplastic with strain hardening. At 400°C and 600°C , softening is always present, even if in small amounts (Figures 5a and 5b). At 800°C , the model predicts mostly hardening followed by perfect viscoplasticity almost independently of the confinement (Figure 5c).

During elastic loading, the ratio between maximum and minimum deviatoric strain is constant and equals 1, so that the deformation is homogeneous within the entire sample (Figure 5). The loss of proportionality ($\bar{\epsilon}_D > 1$) implies nonhomogeneous deformation and its onset loading level (or strain) decreases with increasing temperature and decreasing confinement. The rate at which nonuniformity grows decreases with confinement and with temperature; that is, localization develops more slowly as the ductile regime is

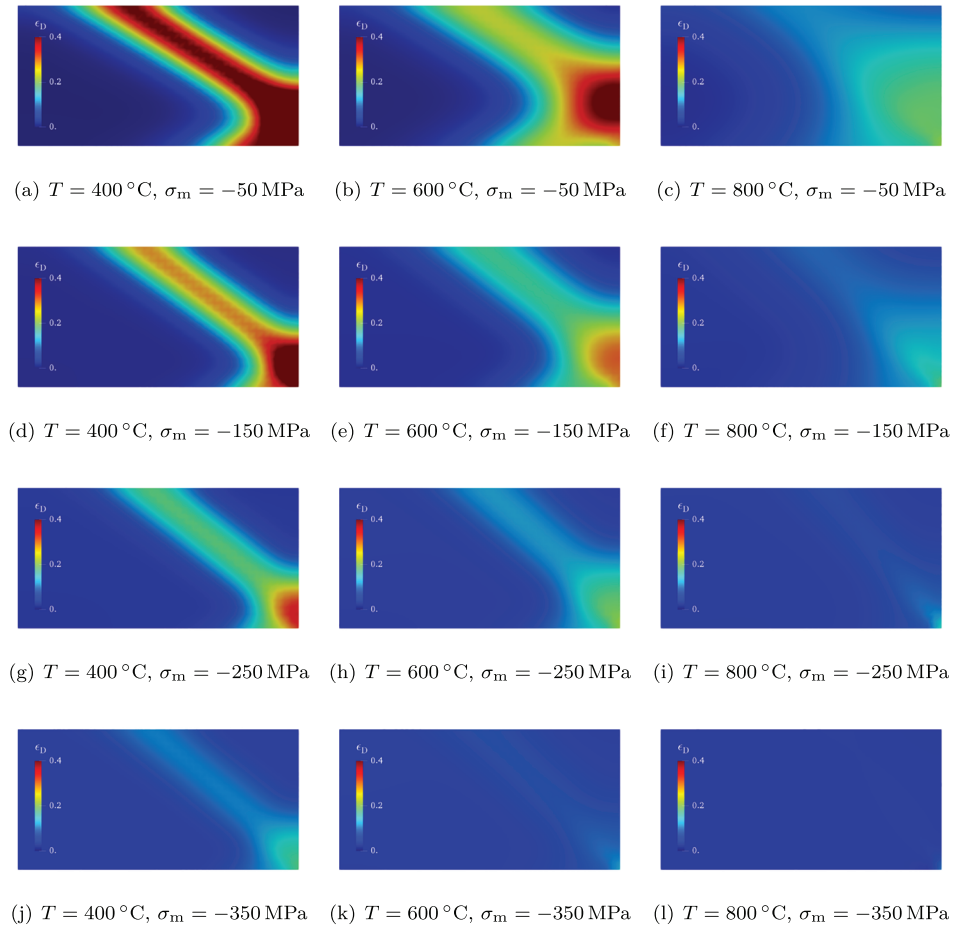


Figure 4. Contour plots of the deviatoric strain at ϵ_{xx} , $t = 0.08$ and at different temperature and confining stress (a–l). Localized deformation patterns are more clear at lower temperature and pressure and indicate a brittle-like behavior.

approached. The quantitative assessment of localization can also detect localized patterns that are not visually obvious: At conditions of $\sigma_m = -350\text{ MPa}$ and $T = 800^{\circ}\text{C}$, the contour map of deviatoric deformation does not show any particular localized deformation trend (Figure 4l), while the quantitative assessment of localization yields for the same conditions $\bar{\epsilon}_D > 1$ (Figure 5c), which is indicative of deviatoric flow around the introduced material weakness.

The difference between minimum and maximum deviatoric strain spans almost 2 orders of magnitude at different environmental conditions. Plotting $\bar{\epsilon}_D$ at $\delta_x = 0.0016\text{ m}$ as a function of confinement, and for a fixed temperature, shows a power law trend of the localized strain measure (Figure 6a). Through interpolation of the numerical data, we built a functional relation of localization with environmental variables $\bar{\epsilon}_D = f(\sigma_m, T)$. The relationship shows a marked increase of localization toward the brittle corner where $\sigma_m \leq 100\text{ MPa}$ and $T \leq 500^{\circ}\text{C}$, while its gradients points toward a simultaneous increase of temperature and pressure (Figure 6b).

4.3. Loading-Unloading-Reloading Path and Fault Locking

We study the behavior under nonmonotonic loading paths, in particular the influence of loading-unloading cycles on previously created localized fractures. For this purpose, a simulation is performed at $T = 700^{\circ}\text{C}$ with the following loading path: (i) confinement is increased to 50 MPa, (ii) a deviatoric stress is applied by uniaxial deformation under constant confinement, (iii) the uniaxial deformation is removed and the sample confined to 300 MPa, and (iv) a new deviatoric phase is applied.

Figure 7a shows the mechanical response during loading-unloading-reloading path at 700°C and at two subsequent confining pressures of 50 and 300 MPa. During the first loading phase the sample exhibits a linear

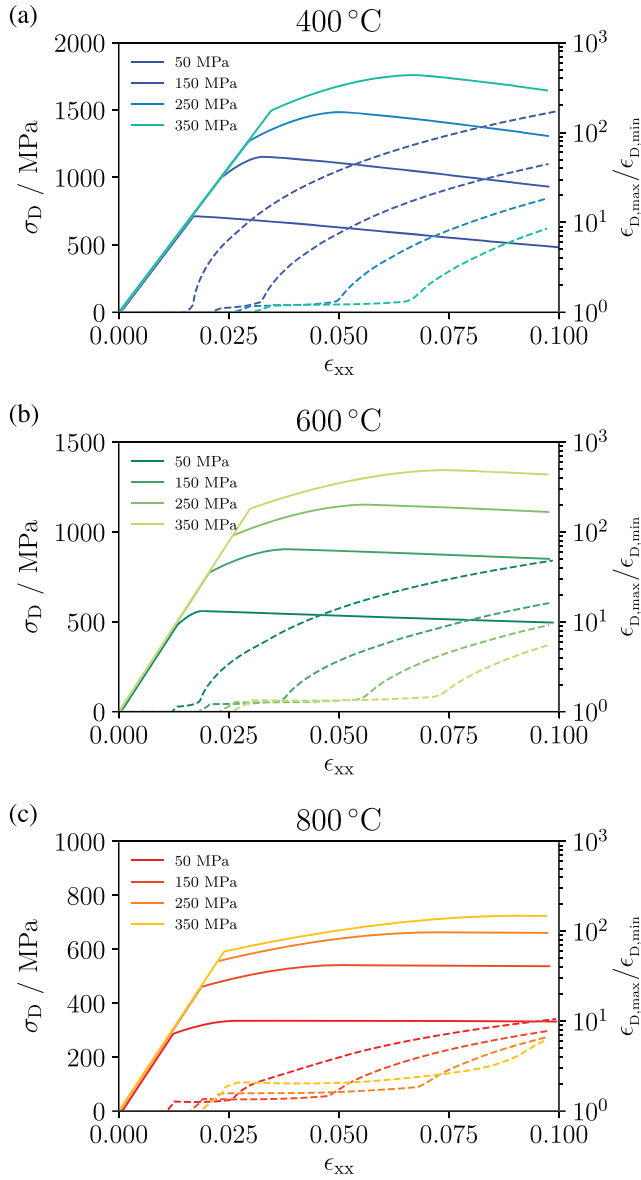


Figure 5. Triaxial compression with constant displacement rate loading conditions at 400°C (a), 600°C (b), and 800°C (c). Solid lines represent the horizontal strain versus deviatoric stress, and dashed lines indicate the ratio between maximum and minimum deviatoric strain $\epsilon_{D, \max}/\epsilon_{D, \min}$, where the statistic is computed on the whole sample and measures localization.

where the equivalent strain is

with

$$\epsilon_{eq, f} = \frac{2}{3} \sqrt{3I_{2D}}, \quad (28)$$

$$I_{2D} = \frac{1}{2} \epsilon : \epsilon - \frac{(\text{tr} \epsilon)^2}{6}, \quad (29)$$

and the equivalent stress $\sigma_{eq} = \sigma_D$, such that the work conjugacy is respected via $\dot{W} = \sigma_{eq} \dot{\epsilon}_{eq}$.

elastic increase before plastic strain hardening is activated. At deformation past the first peak of stress, strain progressively localizes within the sample, as evidenced by the deformation contour maps and by the loss of proportionality between global strain $\epsilon_{xx, t}$ and strain measured at a point within the sample where no localization takes place (off-fault strain $\epsilon_{xx, m}$). The loss of proportionality implies that strain increase and loading happens mostly in the newly created localized zone, where damage and plasticity degrade the material: This can be viewed as the onset of a fault. Once the sample confinement is increased to 300 MPa and reloading takes place, the total and matrix strain are once again proportional until the stress in the sample overcomes the available strength. A new peak of deviatoric stress is reached and the deformation localizes once more within the fracture. The matrix strain rate becomes constant as part of the model undergoes neutral loading conditions, while the localized deformation increases within the sample. This is considered as a reactivation of the fault at a higher confinement. The mechanical response during loading-unloading-reloading under increasing confinement is in qualitative agreement with laboratory observations (Meyer et al., 2019).

5. Energy Dissipation and Strain Rate on Brittleness/Ductility

The model predicts a softening to hardening transition and eventually ideal flow-type behavior and a strength decrease with increasing temperature and pressure. This translates into a shift of energy dissipation from the damage to the viscoplastic mechanism. Absolute dissipated energies would be a misleading indicator, because they both are a function of the strength, which can either decrease or increase when approaching ductile deformation. The plastic surface is formulated in terms of damage effective stress and, during a triaxial loading test, the stress path is viscoelastic until the yield surface is reached and hardening is activated (Figure 8a). Damage is then responsible for strength and stiffness degradation and while it leads to softening at lower temperature, a hardening response occurs with an increase in temperature (Figure 8b). An analogous effect is expected in terms of confinement. Figure 8b shows that the difference between deviatoric damage-effective and total stress tends to disappear when the material deforms in a ductile way. This principle is used to formulate an energy-based brittle-ductile indicator. We can define the damage-effective deviatoric stress dissipated energy as

$$A_T = \int_0^{\epsilon_{eq, f}} \tilde{\sigma}_{eq}(\tau) d\tau, \quad (26)$$

and the damage-total deviatoric stress dissipated energy as

$$A_1 = \int_0^{\epsilon_{eq, f}} \sigma_{eq}(\tau) d\tau, \quad (27)$$

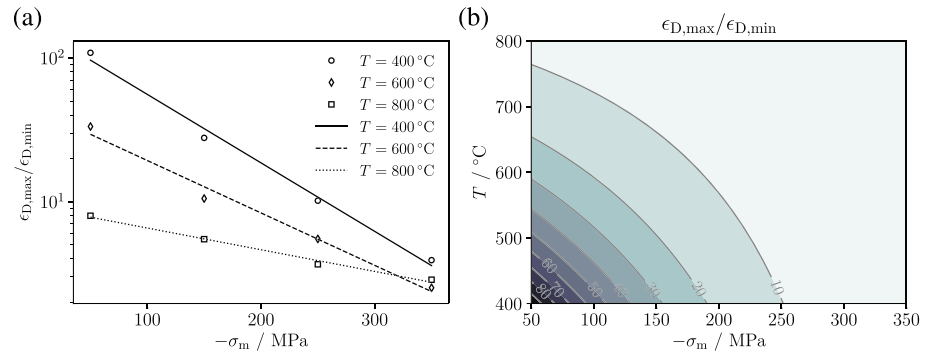


Figure 6. The localization variable $\bar{\epsilon}_D$ at a fixed gross deformation exhibits a power law behavior as a function of confinement σ_m (a). Localization is plotted as an interpolated function of the environmental variables map and shows a trend toward homogeneous deformation in the ductile regimes (b).

The difference between the total and effective stress dissipation is $A_2 = A_T - A_1$ (Figure 8c). Here, we apply as a brittle/ductile indicator the ratio A_2/A_1 . Toward ductile conditions, $A_2/A_1 \rightarrow 0$ because the total and damage effective stress response coincide, since no damage accumulation takes place. During the deformation process, the ratio A_2/A_1 remains low when the material is ductile, while it increases when it behaves in a more brittle manner (Figure 8d). We perform several simulations of material point behavior in triaxial conditions to thoroughly map the temperature and pressure space. The triaxial simulations are performed at different loading rates, representative of fast ($\dot{\epsilon} = 10^{-5} \text{ s}^{-1}$) and slow deformation ($\dot{\epsilon} = 10^{-14} \text{ s}^{-1}$). The energy ratio is mapped through a grid of different normal stress (which translates into an initial confinement σ_m) and temperature.

The energy ratio map (Figure 9) shows a transition from values of A_2/A_1 close to 1 at lower stress and temperature to values close to 0 at higher stress and temperature. The former corresponds to the limiting case of brittle behavior, while the latter to the other limiting case of ductile behavior and pure viscoplastic dissipation. The solid black line corresponds to the ideal BDT, which is here assumed as an arbitrary threshold value of the energy ratio equals to 0.05. At high shear strain rate (10^{-5} s^{-1}) the transition is almost linear in the $\sigma_m - T$ space and the transition temperature decreases with increasing stress (Figure 9a). At lower shear strain rate (10^{-14} s^{-1}), closer to tectonic value, the transition temperature is nonlinear at lower confinement, while it is practically independent of the confinement at $\sigma_m \geq 200 \text{ MPa}$ (Figure 9b). The lower

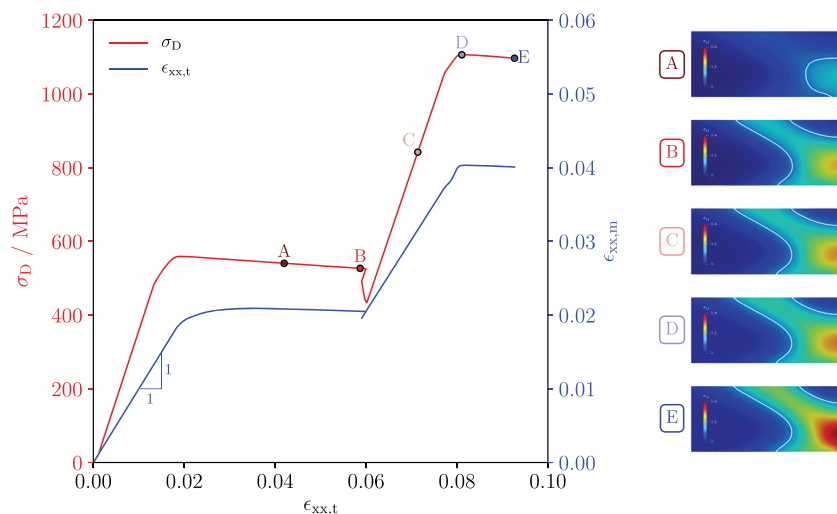


Figure 7. Triaxial compression with loading-unloading-reloading cycle with increasing confinement at 700°C . The contour plots show the lateral deformation at different values of $\epsilon_{xx,t}$ for the inclusion case. The strain within the sample outside the localized strain area is also plotted.

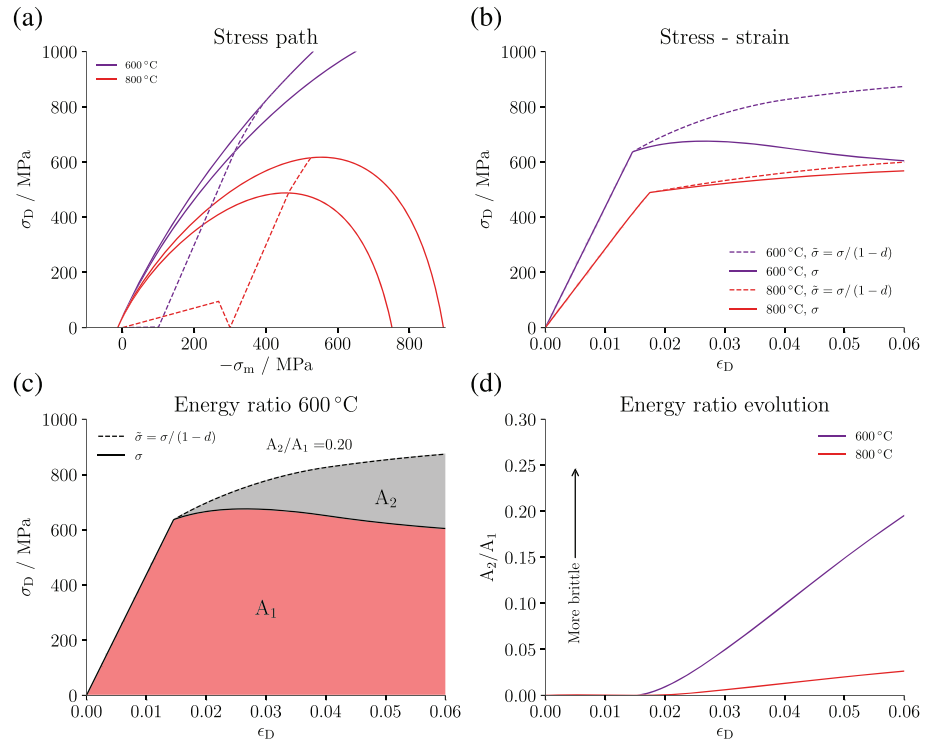


Figure 8. Schematic representation of ductility and brittleness in terms of dissipated energy per unit volume. The plastic surface is formulated in terms of damage effective stress (a), and the hardening/softening response depends on temperature (b) and mean stress. The relative dissipated energy per unit volume between effective and total damage stress allows to remove the relative influence of strength from the brittle-ductile indication (c). A higher energy ratio A_2/A_1 implies more brittleness (d).

deformation rate lowers the transition temperature and simultaneously reduces the influence of confinement due to the dominance of pressure-independent viscous creep in the high-confinement region.

6. The BDT Depth

From the energy ratio map of Figure 9, we extract the BDT in the $\sigma_m - T$ space and, for a given geothermal gradient and mean stress evolution in the crust to compute the BDT depth (Figure 10). We apply the following assumptions: (i) the vertical total stress σ_v is a function of density of the rock, assumed as $\rho = 2,700 \text{ kg m}^{-3}$; (ii) the pore pressure corresponds to the weight of the hydrostatic water column, assuming density changes of water with pressure and temperature; and (iii) normal faulting stress regime with both horizontal total stress components equal to $\sigma_H = \sigma_h = 0.7\sigma_v$. Based on these assumptions and on the interpolated

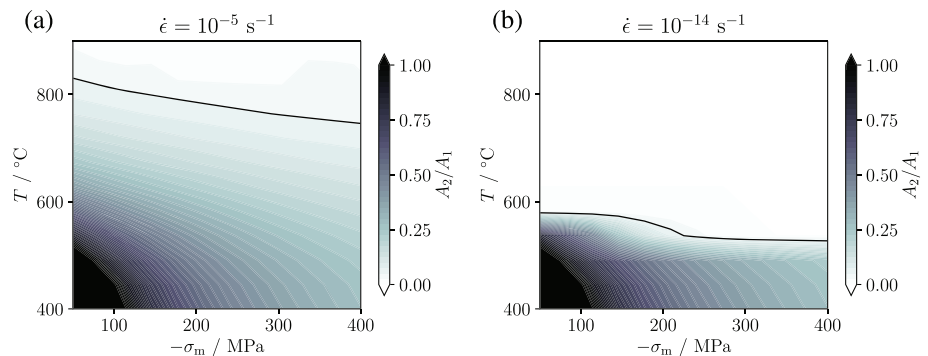


Figure 9. Energy ratio map for rapid (a) and slow (b) shear deformation. The brittle-ductile transition is defined at an energy ratio $A_2/A_1 = 0.05$ and is a function of temperature, mean stress, and strain rate during shear deformation.

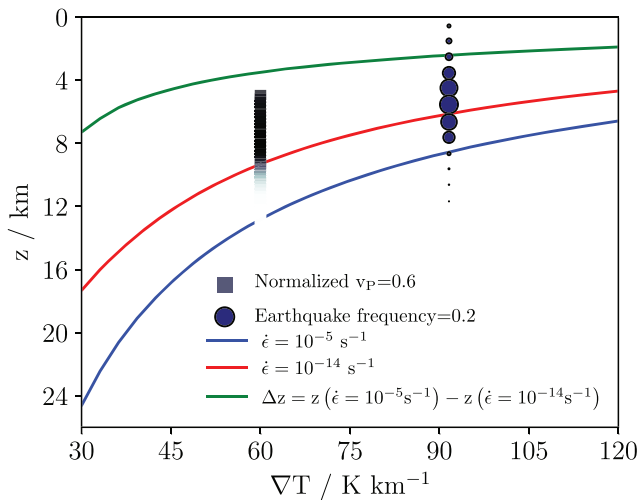


Figure 10. Depth of the brittle-ductile transition as a function of the geothermal gradient. The full dots represent the relative earthquake frequency at a given depth at Reykjanes, Iceland (Friðleifsson et al., 2014), while the square colors represent the P wave velocity computed from the model of Carcione et al. (2018). The depth of the brittle-ductile transition increases at lower geothermal gradient and at higher strain rate. The difference in BDT depth for high and low strain rates is shown by the green curve.

to obtain the results of Figure 10, we compute the evolution of temperature, pore pressure, and poromechanical effective stress with depth. From the previous calculations, we can therefore plot the dissipated energy ratio A_2/A_1 and the localization indicator $\bar{\epsilon}_D$ evolution with depth at the Reykjanes site. We assume that $A_2/A_1 \leq 0.05$ corresponds to ductile deformation and that $\bar{\epsilon}_D \leq 10$ implies diffused deformation. Results show a vertical profile divided into three separate regions: (i) a shallower region in which the brittle behavior is superposed to localized deformation, (ii) an intermediate zone that corresponds to brittle and diffused deformation, and (iii) a deeper part in which the rock deforms in a ductile and diffused way. According to the model, brittleness and ductility are mostly related to the energy dissipation mechanism, which is a concept independent of the localization behavior. The latter, in turn, is simply an expression of the inhomogeneity or concentration of the deformation (rate). In many settings, however, the two phenomena occur in combination, as the ratio of energy dissipation influences the appearance of localized deformation, but it can occur that the softening, damage-driven deformation (brittle) occurs at very low levels of localization (diffused) (Karato, 2008): This is what we have called the brittle-diffused regime.

The earthquake frequency data observed in Reykjanes are primarily prevalent in the regions of brittle-localized to brittle-diffuse deformation patterns. Although the diffused deformation might prevent the formation of fractures and faults in the first place, the rock's deformation is still brittle as a consequence of damage-related dissipation. Below the brittle-diffused to ductile-diffused transition, the earthquake relative frequency falls to below 3% and the deformation becomes essentially aseismic as a consequence of the purely plastic dissipation in a diffused mode. In other words, fracturing, shear banding and stress drops do not occur below this depth.

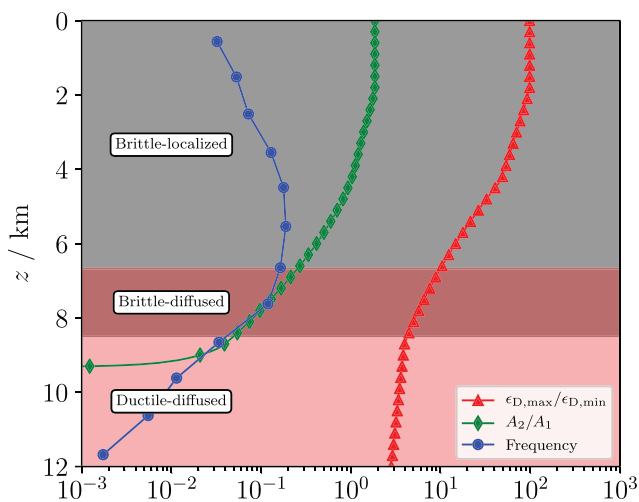


Figure 11. A model of the basaltic rheology below Reykjanes, Iceland. The localization and dissipation thresholds introduce different sections in which the deformation can be brittle-localized, brittle-diffused, or ductile-diffused. The recorded relative earthquake frequency (Friðleifsson et al., 2014) decreases at the onset of homogeneous deformation and becomes negligible at the limit of brittle to ductile deformation.

7. Discussion

The localization of strain depends on how the environmental variables affect the constitutive response of the material. Numerical results have shown that localized strain patterns gradually turn into diffusive

deformation modes with confinement and temperature increase. Although brittle behavior is usually associated with localization, we have shown that under certain conditions brittle (damage) behavior and diffused deformation can occur simultaneously. The introduction of noise in the form of a lower-strength inclusion in the sample gives rise to strain concentrations triggering localized strain behavior (a max-min ratio up to 6) even at what would normally be considered ductile deformation conditions. Since inclusions, weak spots, and heterogeneities are likely to be ubiquitous in the Earth's crust, we believe that this assumption well represents the actual conditions. Laboratory experiments have also confirmed that a single inclusion could trigger localized shear strain under pressure and temperature conditions that would instead lead to homogeneous strain patterns in homogeneous samples (Nardini et al., 2018) and large deformation creep models have shown the necessity of including strain-softening in order to agree with the observations (Döhmann et al., 2019). Nevertheless, localization is possible in nonassociated plasticity and is triggered by the appearance of singularities in the acoustic tensor (Grassl & Jirásek, 2006; Rudnicki & Rice, 1975), themselves associated with acceleration waves (Lemaitre et al., 2009).

Through a wing-crack propagation model, Horii and Nemat-Nasser (1986) have characterized ductility through a parameter $\Delta = K_{Ic}/(\tau_Y\sqrt{\pi c})$, where K_{Ic} is the critical stress intensity factor in Mode-I, τ_Y is the plastic yield strength, and c the half-length of the initial wing crack. The argument is that K_{Ic} increases with temperature while τ_Y decreases (Horii & Nemat-Nasser, 1986), leading to an overall increase of Δ : For a given stress ratio (i.e., confinement), an increase in Δ corresponds to a higher ductility in the deformation mode. In the model we propose, we have assumed the ratio of inelastic dissipation between damage and viscoplasticity as an indicator of ductility. At higher stresses and temperature, the dissipated energy ratio increases while the strength decreases, indicating that the our arguments are based on equivalent considerations as employed by Horii and Nemat-Nasser (1986): Ductility is a ratio between dissipated energy through fracturing processes (damage in our case, which represents microcracking that induces stiffness degradation) and (visco)plastic deformation.

Experimental evidence on marble has shown a progressive frictional locking of a newly created fault in laboratory size samples with the increase of confining pressure, hence ductility (Meyer et al., 2019). The ratio between matrix and fault strain deformation increases progressively as the fault is locked (Meyer et al., 2019). The results of our simulation (Figure 7) exhibit a similar behavior in that at increased confinement, the damaged zone (fault) is locked, the deviatoric yield stress in the material is increased, and, once failure is triggered in the second phase, deformation expands once more from the localized zone into the matrix. A shortcoming of our model is its inability to account for complete frictional locking of the fault, as softening occurs at second onset of failure. Accounting for frictional resistance might be achieved by modeling damage as a tensorial (Qi et al., 2016) or directional quantity (Allix et al., 1995), although higher-order damage models are complex to handle and require extensive experimental testing to calibrate.

The occurrence of natural seismicity is an indicator of the deformation mode in the Earth's crust: A high density of faults and fractures typical of the brittle crust is necessary for seismic events to take place. Although several models that correlate the BDT to seismic behavior concentrate on faults and weak plane mechanics (Aharonov & Scholz, 2019; Shimamoto & Noda, 2014), it has been recognized that the strength of the intact rock plays a fundamental role in determining the overall seismic cycle (Ohnaka, 2013). Patches of strong rock, which can be located between fault segments or as fracture asperities, accumulate strain energy and control the propagation of seismic waves. Mixed-mode fracture and frictional resistance are likely two manifestations of a common elastobrittle behavior that can be unified by introducing adequate characteristic length scales (Ohnaka, 2003). At ductile deformation conditions, seismic wave velocity is attenuated (Carcione et al., 2018) and, combined with lower fracture density, a marked reduction of seismicity is usually observed at the BDT.

The model predicts that the depth of the BDT is strongly influenced by the strain rate. Although crustal strain rate is normally measured in the range of 10^{-18} to 10^{-12} s^{-1} (Molnar, 2020), several other processes can potentially trigger higher deformation rate exceeding 10^{-8} s^{-1} and alter the extent of the previously observed seismogenic crust: Such processes are, for example, dike and sills intrusions, seismic waves, and slow slip events in subduction zones, landslides, hydrothermal explosions, and man-induced processes linked to geothermal energy extraction activities of drilling and fluid production/injection. A ductile crust under tectonic strain rate will not necessarily remain ductile when deformed at higher strain rate.

Increasing the strain rate can push deeper into the crust the location at which brittle phenomena are observed, which could explain the sinking profile of induced seismicity when compared to natural events (Johnson et al., 2016; Yoshioka et al., 2019) or the reactivation of previously aseismic sections of the crust (Friðleifsson et al., 2018). Prior to the drilling of the IDDP-2 well in the Reykjanes Peninsula, Iceland, a small number of earthquakes were observed at depths between 3 and 6 km. During drilling, several earthquakes were observed between 3 and 5 km, with a third of the total account located within ~ 1 km from the well (Friðleifsson et al., 2018). Higher strain rates attained during drilling and colder temperatures induced by wellbore quenching are believed to be the reason for the seismicity increase in a previously aseismic part of the crust (Friðleifsson et al., 2018).

In volcanic areas, the high geothermal gradient causes the crust to deform in a ductile way at lower depth than compared to the cold crust. For example, during the 2015 rifting episode at Bárðarbunga, Iceland, which preceded a volcanic eruption, the seismic signal associated with a propagating dike episode has shown a lower bound at a depth of ~ 6 km, which has been interpreted as the depth of the BDT (Ágústsdóttir et al., 2019). Being a volcanic area with a high geothermal gradient (presumably $>100 \text{ K km}^{-1}$), our model predicts a depth of the BDT associated with the diking event that is in good agreement with the observations.

The various deformation modes of a rock have several implications for the exploitation of deep geothermal systems in volcanic areas, the so-called supercritical geothermal systems. Borehole stability (Kruszewski & Wittig, 2018) and reservoir operations (Friðleifsson et al., 2018; Parisio et al., 2019) are expected to be affected by the rheology of the rock. During long-term fluid reinjection in supercritical geothermal systems, cooling dominates the seismic response (Parisio et al., 2019) and a transition from more ductile to more brittle behavior will also increase the risk of brittle faulting and additional seismicity. The rheology and heterogeneity of the rock controls the deformation patterns that lead to strain localization and the formation of discrete fractures and faults. Fractures, in turn, are a fundamental control in the heat and mass transport in the crust (Ingebritsen et al., 2010), such that a strong link between rock rheology and poromechanical behavior is expected. Laboratory experiments have shown that permeable fractures are most likely present beyond what was previously considered as a limiting temperature of $\sim 400^\circ\text{C}$ for permeability (Watanabe et al., 2017): Here we show that for basalt, it could be expected that fractures and shear zones form at temperatures $\geq 600^\circ\text{C}$ (Adelinet et al., 2013; Molnar, 2020), especially at higher than tectonic strain rates (10^{-5} s^{-1} in this case). Nonetheless, a complete rheology-permeability relationship is still to be devised as, in general, are models that take into account the coupled effects of moving fluids (Benson et al., 2008), the reduction of strength in saturated conditions (Karato & Wong, 1995), and the decreased hydraulic transmissivity at high temperature (Watanabe et al., 2017).

8. Conclusions

Our predictions of the depth of the BDT agree well with observations of volcanic events (Ágústsdóttir et al., 2019; Sigmundsson et al., 2015) and natural (Blanck et al., 2019) and drilling-induced seismicity (Friðleifsson et al., 2018) in Iceland, where basalt is extensively present as the main lithology. The model results are in good agreement with experimental evidence (Adelinet et al., 2013; Döhmman et al., 2019; Meyer et al., 2019; Nardini et al., 2018; Violay et al., 2012, 2017), in situ observations (Ágústsdóttir et al., 2019; Friðleifsson et al., 2014, 2017), and theoretical arguments (Carcione et al., 2018; Horii & Nemat-Nasser, 1986; Parisio et al., 2019). The approach taken can be extended to study other lithologies such as carbonatic basements in which the depth of the BDT would be shallower (Parisio et al., 2019), or above-average geothermal gradient around local temperature anomalies, such as shallow-depth magma pockets (Elders et al., 2014).

The definition of brittle and ductile deformation is essentially connected to irreversible and path-dependent behavior: It seems adequate to interpret the BDT as a material process that evolves with the environmental and loading conditions and with the fluctuations of the material structure. Our results confirm that the BDT should not be seen as a static property of the subsurface but instead as a dynamical property that is the result of articulated and complex rheological features influencing the mechanical response, which ultimately depend upon stress conditions, loading rate, temperature, and the presence of heterogeneities. Accordingly, we have shown the deformation mechanisms that could explain earthquakes occurring at $T \geq 600^\circ\text{C}$ (Molnar, 2020).

Data Availability Statement

The entire OpenGeoSys source code employed for the analyses is freely available online (at <https://gitlab.opengeosys.org/ogs/ogs>).

Acknowledgments

The contribution of F. P. was funded by the Deutsche Forschungsgemeinschaft (DFG, German Research Foundation), project number PA 3451/1-1. We thank Thomas Helfer (CEA, France) for support and gratefully acknowledge the contributions of the OpenGeoSys developer team. Open access funding enabled and organized by Projekt DEAL.

References

- Adelinet, M., Fortin, J., Schubnel, A., & Guéguen, Y. (2013). Deformation modes in an Icelandic basalt: From brittle failure to localized deformation bands. *Journal of Volcanology and Geothermal Research*, 255, 15–25.
- Ágústssdóttir, T., Winder, T., Woods, J., White, R. S., Greenfield, T., & Brandsdóttir, B. (2019). Intense seismicity during the 2014–2015 Bárðarbunga-Holuhraun rifting event, Iceland, reveals the nature of dike-induced earthquakes and caldera collapse mechanisms. *Journal of Geophysical Research: Solid Earth*, 124, 8331–8357. <https://doi.org/10.1029/2018JB016010>
- Aharonov, E., & Scholz, C. H. (2019). The brittle-ductile transition predicted by a physics-based friction law. *Journal of Geophysical Research: Solid Earth*, 124, 2721–2737. <https://doi.org/10.1029/2018JB016878>
- Allix, O., Ladeveze, P., & Corigliano, A. (1995). Damage analysis of interlaminar fracture specimens. *Composite Structures*, 31(1), 61–74.
- Armero, F., & Garikipati, K. (1996). An analysis of strong discontinuities in multiplicative finite strain plasticity and their relation with the numerical simulation of strain localization in solids. *International Journal of Solids and Structures*, 33(20–22), 2863–2885.
- Bakker, R. R., Violay, M. E., Benson, P. M., & Vinciguerra, S. C. (2015). Ductile flow in sub-volcanic carbonate basement as the main control for edifice stability: New experimental insights. *Earth and Planetary Science Letters*, 430, 533–541.
- Benson, P. M., Vinciguerra, S., Meredith, P. G., & Young, R. P. (2008). Laboratory simulation of volcano seismicity. *Science*, 322(5899), 249–252.
- Bilke, L., Flemisch, B., Kalbacher, T., Kolditz, O., Helmig, R., & Nagel, T. (2019). Development of open-source porous media simulators: Principles and experiences. *Transport in Porous Media*, 130, 337–361.
- Blanck, H., Jousset, P., Hersir, G. P., Ágústsson, K., & Flóvenz, O. G. (2019). Analysis of 2014–2015 on-and off-shore passive seismic data on the Reykjanes Peninsula, SW Iceland. *Journal of Volcanology and Geothermal Research*, 391, 106548.
- Brantut, N., Heap, M. J., Meredith, P. G., & Baud, P. (2013). Time-dependent cracking and brittle creep in crustal rocks: A review. *Journal of Structural Geology*, 52, 17–43.
- Carcione, J. M., Poletto, F., & Farina, B. (2018). The Burgers/squirt-flow seismic model of the crust and mantle. *Physics of the Earth and Planetary Interiors*, 274, 14–22.
- Caristan, Y. (1982). The transition from high temperature creep to fracture in Maryland diabase. *Journal of Geophysical Research*, 87(B8), 6781–6790.
- de Borst, R., & Heeres, O. M. (2002). A unified approach to the implicit integration of standard, standard and viscous plasticity models. *International Journal for Numerical and Analytical Methods in Geomechanics*, 26(11), 1059–1070.
- de Borst, R., & Verhoosel, C. V. (2016). Gradient damage vs phase-field approaches for fracture: Similarities and differences. *Computer Methods in Applied Mechanics and Engineering*, 312, 78–94.
- Döhrmann, M. J., Brune, S., Nardini, L., Rybacki, E., & Dresen, G. (2019). Strain localization and weakening processes in viscously deforming rocks: Numerical modeling based on laboratory torsion experiments. *Journal of Geophysical Research: Solid Earth*, 124, 1120–1137. <https://doi.org/10.1029/2018JB016917>
- Duretz, T., de Borst, R., Yamato, P., & Le Pourhiet, L. (2020). Toward robust and predictive geodynamic modeling: The way forward in frictional plasticity. *Geophysical Research Letters*, 47, e2019GL086027. <https://doi.org/10.1029/2019GL086027>
- Elders, W. A., Friðleifsson, G., & Albertsson, A. (2014). Drilling into magma and the implications of the Iceland Deep Drilling Project (IDDP) for high-temperature geothermal systems worldwide. *Geothermics*, 49, 111–118.
- Evans, B., Fredrich, J. T., & Wong, T.-F. (1990). The brittle-ductile transition in rocks: Recent experimental and theoretical progress. In *The brittle-ductile transition in rocks, Geophysical Monograph Series* (Vol. 56, pp. 1–20). Washington, DC: American Geophysical Union.
- Friðleifsson, G., Elders, W., & Albertsson, A. (2014). The concept of the Iceland deep drilling project. *Geothermics*, 49, 2–8.
- Friðleifsson, G., Elders, W. A., Zierenberg, R. A., Fowler, A. P. G., Weisenberger, T. B., Mesfin, K. G., et al. (2018). The Iceland Deep Drilling Project at Reykjanes: Drilling into the root zone of a black smoker analog. *Journal of Volcanology and Geothermal Research*, 391, 106435.
- Friðleifsson, G., Elders, W., Zierenberg, R., Stefánsson, A., Fowler, A., Weisenberger, T. B., et al. (2017). The Iceland Deep Drilling Project 4.5 km deep well, IDDP-2, in the seawater-recharged Reykjanes geothermal field in SW Iceland has successfully reached its supercritical target. *Scientific Drilling*, 23, 1–12.
- Grassl, P., & Jirásek, M. (2006). Damage-plastic model for concrete failure. *International Journal of Solids and Structures*, 43(22), 7166–7196.
- Guy, N., Seyedi, D., & Hild, F. (2018). Characterizing fracturing of clay-rich lower wondrous rock: From laboratory experiments to nonlocal damage-based simulations. *Rock Mechanics and Rock Engineering*, 51(6), 1777–1787.
- Hartlieb, P., Toifl, M., Kuchar, F., Meisels, R., & Antretter, T. (2016). Thermo-physical properties of selected hard rocks and their relation to microwave-assisted comminution. *Minerals Engineering*, 91, 34–41.
- Heap, M. J., Mollo, S., Vinciguerra, S., Lavallée, Y., Hess, K.-U., Dingwell, D. B., et al. (2013). Thermal weakening of the carbonate basement under Mt. Etna volcano (Italy): Implications for volcano instability. *Journal of Volcanology and Geothermal Research*, 250, 42–60.
- Helfer, T. (2019). MGIS. <https://github.com/thelfer/MFrontGenericInterfaceSupport>, original-date: 2018-06-20T12:41:49Z.
- Helfer, T., Bleyer, J., Frondelius, T., Yashchuk, I., Nagel, T., & Naumov, D. (2020). The MFrontGenericInterfaceSupport project. *Journal of Open Source Software*, 5(48), 2003.
- Helfer, T., Michel, B., Proix, J.-M., Salvo, M., Sercombe, J., & Casella, M. (2015). Introducing the open-source mfront code generator: Application to mechanical behaviours and material knowledge management within the PLEIADES fuel element modelling platform. *Computers & Mathematics with Applications*, 70(5), 994–1023.
- Hobbs, B. E., Mühlhaus, H.-B., & Ord, A. (1990). Instability, softening and localization of deformation. *Geological Society, London, Special Publications*, 54(1), 143–165.
- Hori, H., & Nemat-Nasser, S. (1986). Brittle failure in compression: Splitting faulting and brittle-ductile transition. *Philosophical Transactions of the Royal Society of London. Series A, Mathematical and Physical Sciences*, 319(1549), 337–374.
- Ingebritsen, S., Geiger, S., Hurwitz, S., & Driesner, T. (2010). Numerical simulation of magmatic hydrothermal systems. *Reviews of Geophysics*, 48, RG1002. <https://doi.org/10.1029/2009RG000287>
- Jacquet, A. B., & Cacace, M. (2020). Multiphysics modeling of a brittle-ductile lithosphere: 2. Semi-brittle, semi-ductile deformation and damage rheology. *Journal of Geophysical Research: Solid Earth*, 125, e2019JB018475. <https://doi.org/10.1029/2019JB018475>

- Johnson, C. W., Totten, E. J., & Bürgmann, R. (2016). Depth migration of seasonally induced seismicity at The Geysers geothermal field. *Geophysical Research Letters*, 43, 6196–6204. <https://doi.org/10.1002/2016GL069546>
- Karato, S.-i. (2008). *Deformation of Earth materials: An introduction to the rheology of solid Earth*, vol. 463: Cambridge University Press.
- Karato, S.-i., & Wong, T.-f. (1995). Rock deformation: Ductile and brittle. *Reviews of Geophysics*, 33(S1), 451–457.
- Kato, A., Yoshida, S., Ohnaka, M., & Mochizuki, H. (2004). The dependence of constitutive properties on temperature and effective normal stress in seismogenic environments. *Pure and Applied Geophysics*, 161(9–10), 1895–1913.
- Kolditz, O., Bauer, S., Bilke, L., Böttcher, N., Delfs, J. O., Fischer, T., et al. (2012). OpenGeoSys: An open-source initiative for numerical simulation of thermo-hydro-mechanical/chemical (THM/C) processes in porous media. *Environmental Earth Sciences*, 67(2), 589–599.
- Kronenberg, A. K., & Shelton, G. L. (1980). Deformation microstructures in experimentally deformed Maryland diabase. *Journal of Structural Geology*, 2(3), 341–353.
- Kruszewski, M., & Wittig, V. (2018). Review of failure modes in supercritical geothermal drilling projects. *Geothermal Energy*, 6(1), 28.
- Kumari, W., Ranjith, P., Perera, M., Shao, S., Chen, B., Lashin, A., et al. (2017). Mechanical behaviour of Australian strathbogie granite under in-situ stress and temperature conditions: An application to geothermal energy extraction. *Geothermics*, 65, 44–59.
- Lamur, A., Kendrick, J., Eggertsson, G., Wall, R., Ashworth, J., & Lavallée, Y. (2017). The permeability of fractured rocks in pressurised volcanic and geothermal systems. *Scientific Reports*, 7(1), 1–9.
- Lavallée, Y., Heap, M. J., Kendrick, J. E., Kueppers, U., & Dingwell, D. B. (2019). The fragility of Volcán de Colima material constraint, *Volcán de Colima* (pp. 241–266): Springer.
- Lemaitre, J., Chaboche, J.-L., Benallal, A., & Desmorat, R. (2009). *Mécanique des matériaux solides-3ème édition*: Dunod.
- Lockner, D., Byerlee, J. D., Kukusenko, V., Ponomarev, A., & Sidorin, A. (1991). Quasi-static fault growth and shear fracture energy in granite. *Nature*, 350(6313), 39–42.
- Lyakhovsky, V., Ben-Zion, Y., & Agnon, A. (1997). Distributed damage, faulting, and friction. *Journal of Geophysical Research*, 102(B12), 27,635–27,649.
- Lyakhovsky, V., Hamiel, Y., & Ben-Zion, Y. (2011). A non-local visco-elastic damage model and dynamic fracturing. *Journal of the Mechanics and Physics of Solids*, 59(9), 1752–1776.
- Marti, S., Stünitz, H., Heilbronner, R., Plümper, O., & Drury, M. (2017). Experimental investigation of the brittle-viscous transition in mafic rocks—Interplay between fracturing, reaction, and viscous deformation. *Journal of Structural Geology*, 105, 62–79.
- Meyer, G. G., Brantut, N., Mitchell, T. M., & Meredith, P. G. (2019). Fault reactivation and strain partitioning across the brittle-ductile transition. *Geology*, 47(12), 1127–1130.
- Molnar, P. (2020). The brittle-plastic transition, earthquakes, temperatures, and strain rates. *Journal of Geophysical Research: Solid Earth*, 125, e2019JB019335. <https://doi.org/10.1029/2019JB019335>
- Nagel, T., Minkley, W., Böttcher, N., Naumov, D., Görke, U.-J., & Kolditz, O. (2017). Implicit numerical integration and consistent linearization of inelastic constitutive models of rock salt. *Computers & Structures*, 182, 87–103.
- Nardini, L., Rybacki, E., Dörmann, M. J., Morales, L. F., Brune, S., & Dresen, G. (2018). High-temperature shear zone formation in Carrara marble: The effect of loading conditions. *Tectonophysics*, 749, 120–139.
- Nguyen, T. H. A., Bui, T. Q., & Hirose, S. (2018). Smoothing gradient damage model with evolving anisotropic nonlocal interactions tailored to low-order finite elements. *Computer Methods in Applied Mechanics and Engineering*, 328, 498–541.
- Odedra, A., Ohnaka, M., Mochizuki, H., & Sammonds, P. (2001). Temperature and pore pressure effects on the shear strength of granite in the brittle-plastic transition regime. *Geophysical Research Letters*, 28(15), 3011–3014.
- Ohnaka, M. (1995). A shear failure strength law of rock in the brittle-plastic transition regime. *Geophysical Research Letters*, 22(1), 25–28.
- Ohnaka, M. (2003). A constitutive scaling law and a unified comprehension for frictional slip failure, shear fracture of intact rock, and earthquake rupture. *Journal of Geophysical Research*, 108(B2), 2080. <https://doi.org/10.1029/2000JB000123>
- Ohnaka, M. (2013). *The physics of rock failure and earthquakes*: Cambridge University Press.
- Pariso, F., & Laloui, L. (2017). Plastic-damage modeling of saturated quasi-brittle shales. *International Journal of Rock Mechanics and Mining Sciences*, 93, 295–306.
- Pariso, F., Tarokh, A., Makhnenko, R., Naumov, D., Miao, X.-Y., Kolditz, O., & Nagel, T. (2019). Experimental characterization and numerical modelling of fracture processes in granite. *International Journal of Solids and Structures*, 163, 102–116.
- Pariso, F., Vilarrasa, V., Wang, W., Kolditz, O., & Nagel, T. (2019). The risks of long-term re-injection in supercritical geothermal systems. *Nature Communications*, 10(1), 1–11.
- Pariso, F., Vinciguerra, S., Kolditz, O., & Nagel, T. (2019). The brittle-ductile transition in active volcanoes. *Scientific Reports*, 9(1), 143.
- Pec, M., Stünitz, H., Heilbronner, R., & Drury, M. (2016). Semi-brittle flow of granitoid fault rocks in experiments. *Journal of Geophysical Research: Solid Earth*, 121, 1677–1705. <https://doi.org/10.1002/2015JB012513>
- Qi, M., Giraud, A., Colliat, J.-B., & Shao, J.-F. (2016). A numerical damage model for initially anisotropic materials. *International Journal of Solids and Structures*, 100, 245–256.
- Reber, J. E., & Pec, M. (2018). Comparison of brittle-and viscous creep in quartzites: Implications for semi-brittle flow of rocks. *Journal of Structural Geology*, 113, 90–99.
- Ross, P.-S., Peate, I. U., McClintock, M., Xu, Y. G., Skilling, I. P., White, J. D., & Houghton, B. F. (2005). Mafic volcanoclastic deposits in flood basalt provinces: A review. *Journal of Volcanology and Geothermal Research*, 145(3–4), 281–314.
- Rudnicki, J. W., & Rice, J. (1975). Conditions for the localization of deformation in pressure-sensitive dilatant materials. *Journal of the Mechanics and Physics of Solids*, 23(6), 371–394.
- Shimamoto, T., & Noda, H. (2014). A friction to flow constitutive law and its application to a 2-D modeling of earthquakes. *Journal of Geophysical Research: Solid Earth*, 119, 8089–8106. <https://doi.org/10.1002/2014JB011170>
- Sigmundsson, F., Hooper, A., Hreinsdóttir, S., Vogfjörð, K. S., Ófeigsson, B. G., Heimisson, E. R., et al. (2015). Segmented lateral dyke growth in a rifting event at Bárðarbunga volcanic system, Iceland. *Nature*, 517(7533), 191–195.
- Simo, J. C., & Ju, J. W. (1987). Strain- and stress-based continuum damage models—I. Formulation. *International Journal of Solids and Structures*, 23(7), 821–840.
- Suh, H. S., Sun, W., & O'Connor, D. (2020). A phase field model for cohesive fracture in micropolar continua. arXiv preprint arXiv:2001.01022.
- Tullis, J., & Yund, R. (1992). The brittle-ductile transition in feldspar aggregates: An experimental study, *International geophysics* (Vol. 51, pp. 89–117): Elsevier.
- Tvergaard, V., & Needleman, A. (1995). Effects of nonlocal damage in porous plastic solids. *International Journal of Solids and Structures*, 32(8–9), 1063–1077.

- Violay, M., Gibert, B., Mainprice, D., & Burg, J.-P. (2015). Brittle versus ductile deformation as the main control of the deep fluid circulation in oceanic crust. *Geophysical Research Letters*, *42*, 2767–2773. <https://doi.org/10.1002/2015GL063437>
- Violay, M., Gibert, B., Mainprice, D., Evans, J.-M., Azais, P., & Pezard, P. (2012). An experimental study of the brittle-ductile transition of basalt at oceanic crust pressure and temperature conditions. *Journal of Geophysical Research*, *117*, B03213. <https://doi.org/10.1029/2011JB008884>
- Violay, M., Heap, M. J., Acosta, M., & Madonna, C. (2017). Porosity evolution at the brittle-ductile transition in the continental crust: Implications for deep hydro-geothermal circulation. *Scientific Reports*, *7*(1), 7705.
- Watanabe, N., Egawa, M., Sakaguchi, K., Ishibashi, T., & Tsuchiya, N. (2017). Hydraulic fracturing and permeability enhancement in granite from subcritical/brittle to supercritical/ductile conditions. *Geophysical Research Letters*, *44*, 5468–5475. <https://doi.org/10.1002/2017GL073898>
- Watanabe, N., Numakura, T., Sakaguchi, K., Saishu, H., Okamoto, A., Ingebritsen, S. E., & Tsuchiya, N. (2017). Potentially exploitable supercritical geothermal resources in the ductile crust. *Nature Geoscience*, *10*(2), 140–144.
- Wong, T.-F. (1982). Effects of temperature and pressure on failure and post-failure behavior of westerly granite. *Mechanics of Materials*, *1*(1), 3–17.
- Yoshioka, K., Parisio, F., Naumov, D., Lu, R., Kolditz, O., & Nagel, T. (2019). Comparative verification of discrete and smeared numerical approaches for the simulation of hydraulic fracturing. *GEM-International Journal on Geomathematics*, *10*(1), 13.
- Yoshioka, K., Pasikki, R., & Stimac, J. (2019). A long term hydraulic stimulation study conducted at the Salak geothermal field. *Geothermics*, *82*, 168–181.
- Zheng, Z., Sun, W., & Fish, J. (2016). Micropolar effect on the cataclastic flow and brittle-ductile transition in high-porosity rocks. *Journal of Geophysical Research: Solid Earth*, *121*, 1425–1440. <https://doi.org/10.1002/2015JB012179>